Electronic structure of RuO_2, OsO_2, and IrO_2

L. F. Mattheiss
Bell Laboratories, Murray Hill, New Jersey 07974
(Received 29 October 1975)

The Slater-Koster linear-combination-of-atomic-orbitals (LCAO) interpolation method is applied to fit the results of nonrelativistic augmented-plane-wave (APW) calculations at symmetry points in the Brillouin zone for several metallic transition-metal dioxides with the rutile structure, namely, RuO_2, OsO_2, and IrO_2. This LCAO model, which involves Bloch sums formed from the oxygen $2s$-$2p$ and metal-atom d orbitals, fits 92 APW energy eigenvalues with a 5-mRy rms error by means of 37 adjustable two-center parameters. The results of this APW-LCAO model are applied to determine the band profiles, density of states, and Fermi surfaces for each of these compounds. It is found that the Fermi-surface topology of these materials is altered significantly by the effects of spin-orbit coupling involving the metal-atom d orbitals. These effects are included in this APW-LCAO band model by means of an additional parameter, the spin-orbit parameter ξ_d. The resulting Fermi surfaces are in good qualitative agreement with those inferred from magnetothermal-oscillation data by Graebner *et al.*

I. INTRODUCTION

The family of transition-metal dioxide compounds with rutile-type structures possess an interesting variety of electrical and magnetic properties. These are summarized in Table I, which is derived from the review articles by Goodenough[1] and Adler.[2] This diversity in physical properties is particularly striking among the $3d$ dioxides, where successive compounds include a large-gap (3 eV) semiconductor (TiO_2), a material that undergoes a metal-semiconductor transition (VO_2), a metallic ferromagnet (CrO_2), and an antiferromagnetic semiconductor (MnO_2).

By comparison, the properties of the $4d$ and $5d$ compounds tend to be less exotic. The main exception is NbO_2, which exhibits a metal-semiconductor transition at 1070 °K. The remaining $4d$ and $5d$ dioxides are found to be metallic and they often crystallize with a distorted rutile-type structure having monoclinic or orthorhombic symmetry. Distorted compounds are found in the d^1, d^2, d^3, and d^6 columns of Table I. Among the undistorted materials are the d^4 compounds RuO_2 and OsO_2 and the d^5 compound IrO_2. The availability of high-quality single-crystal samples of these materials has stimulated a series of experimental studies relating to their band structures and Fermi surfaces. These include de Haas–van Alphen,[3] magnetoresistance,[4,5] cyclotron-resonance,[6] magnetothermal-oscillation,[7] electrical transport,[8] and specific-heat[9] measurements.

Graebner, Ryden, and co-workers[5,7] have proposed detailed Fermi-surface models for RuO_2, OsO_2, and IrO_2 based on their magnetothermal-oscillation and magnetoresistance data as well as the results of a preliminary band-structure calculation for RuO_2 by the present author. In each material, it is found that the Fermi-surface topology is significantly altered by the effects of spin-orbit coupling. This is particularly striking in the magnetothermal-oscillation data[7] for the two d^4 compounds, RuO_2 and OsO_2. In the nonrelativistic limit, one would expect these two isoelectronic compounds to have rather similar Fermi surfaces. However, the observed magnetothermal-oscillation frequencies include only two branches in OsO_2 while at least five separate frequencies are observed in RuO_2.

The purpose of the present investigation is to calculate the band structures and Fermi surfaces for RuO_2, OsO_2, and IrO_2 and to compare these with the available experimental data. These calculations are carried out in two stages. The first stage involves the application of the nonrelativistic augmented-plane-wave (APW) method to determine the energy-band states for these compounds at six symmetry points in the tetragonal Brillouin zone. These APW results are then utilized in the second stage to determine 37 two-center parameters in the Slater-Koster linear-combination-of-atomic-orbitals (LCAO) interpolation method,[10] which is applied to fit the sixteen oxygen $2s$-$2p$ and the ten

TABLE I. Properties of transition-metal-dioxide compounds that form with rutile-type structures. Metals, semiconductors, ferromagnets, and antiferromagnets are identified by *M*, *S*, F, and AF, respectively.

	d^0	d^1	d^2	d^3	d^4	d^5	d^6
$3d$	TiO_2 (*S*)	VO_2[a] (*M*–*S*)	CrO_2 (F-*M*)	MnO_2 (AF-*S*)			
$4d$		NbO_2[a] (*M*-*S*)	MoO_2[a] (*M*)	TcO_2[a] (*M*)	RuO_2 (*M*)	RhO_2 (*M*)	
$5d$		TaO_2 (?)	WO_2[a] (*M*)	ReO_2[a] (*M*)	OsO_2 (*M*)	IrO_2 (*M*)	PtO_2[a] (*M*)

[a]Involves a distorted form of the rutile structure.

metal-atom d bands. The effects of spin-orbit coupling for metal-atom d states are included in the LCAO model by means of a spin-orbit parameter ξ_d. This leads to a 52-by-52 model Hamiltonian matrix with complex elements.

There have been no previous energy-band calculations for these particular compounds with the undistorted rutile structure. Caruthers *et al.*[11] have carried out a similar combined APW-LCAO calculation for metallic VO_2, which has the rutile structure at temperatures above 340 °K. Chatterjee *et al.*[12] have performed limited APW calculations along a single symmetry line (ΓZ) of the Brillouin zone for tetragonal VO_2. The present APW-LCAO results for RuO_2, OsO_2, and IrO_2 are qualitatively similar to those of Caruthers *et al.*[11] for VO_2. However, the results of Chatterjee *et al.*[12] bear little resemblence to those of either calculation.

The details of the present calculations are discussed in Sec. II. These details include the symmetry of the rutile structure as well as various computational features of the APW and LCAO calculations. The results of the present APW-LCAO model for RuO_2, OsO_2, and IrO_2 are presented in Sec. III, including energy-band, density-of-states, and Fermi-surface results. These results are compared with experiment in Sec. IV. Section V contains a brief discussion and summary of these results.

II. DETAILS OF CALCULATION

A. Rutile structure

The primitive unit cell for AB_2 compounds with the rutile structure is shown in Fig. 1(a). The shaded and unshaded spheres represent the A and B atoms, respectively. Each unit cell contains two AB_2 molecules, or a total of six atoms. The Bravais lattice is tetragonal with $c/a < 1$. The corresponding Brillouin zone is shown in Fig. 1(b), where the standard notation is used to identify symmetry points and lines.

The primitive translations for the tetragonal Bravais lattice are generated by the vectors

$$\vec{t}_1 = a\hat{i}, \quad \vec{t}_2 = a\hat{j}, \quad \vec{t}_3 = c\hat{k} \ , \tag{1}$$

where a and c are the lattice parameters and $\hat{i}$, $\hat{j}$, and $\hat{k}$ are unit vectors along the x, y, and z axes, respectively. To simplify the notation, we express general vectors in real space $\vec{r}$ in terms of these units so that

$$\vec{r} \equiv (x, y, z) = x\vec{t}_1 + y\vec{t}_2 + z\vec{t}_3 \ . \tag{2}$$

The corresponding vectors for the reciprocal lattice are

$$\vec{b}_1 = (1/a)\hat{i}, \quad \vec{b}_2 = (1/a)\hat{j}, \quad \vec{b}_3 = (1/c)\hat{k} \ . \tag{3}$$

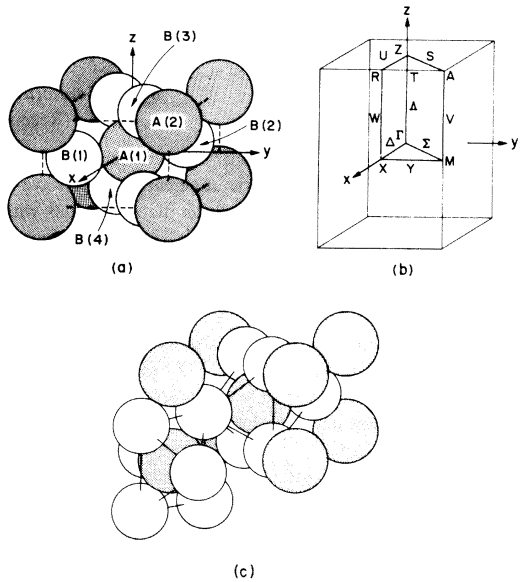

FIG. 1. (a) Primitive unit cell for AB_2 compounds with the rutile structure. (b) Brillouin zone for the tetragonal Bravais lattice with $c/a < 1$. (c) Orientation of octahedral clusters surrounding A atoms at body-centered and corner positions.

Accordingly, a general wave-vector $\vec{k}$ is written

$$\vec{k} \equiv (\xi, \eta, \zeta) = 2\pi(\xi\vec{b}_1 + \eta\vec{b}_2 + \zeta\vec{b}_3) \ . \tag{4}$$

The A atoms in Fig. 1(a) form a body-centered tetragonal lattice. The two A atoms in the unit cell are centered at the positions $\vec{r}_{A1} = (0, 0, 0)$ and $\vec{r}_{A2} = (\frac{1}{2}, \frac{1}{2}, \frac{1}{2})$. The coordinates of the four B atoms are $\vec{r}_{B1} = (u, -u, 0)$, $\vec{r}_{B2} = -\vec{r}_{B1} = (-u, u, 0)$, $\vec{r}_{B3} = (\frac{1}{2} - u, \frac{1}{2} - u, \frac{1}{2})$, and $\vec{r}_{B4} = -\vec{r}_{B3} = (-\frac{1}{2} + u, -\frac{1}{2} + u, -\frac{1}{2})$, respectively, where the position parameter u generally has a value close to 0.31. Each A atom is surrounded by a distorted octahedral array of six B atoms. Neighboring octahedral coordination units share edges along the c axis but only vertices in the basal plane. As shown in Fig. 1(c), the orientation of the octahedra surrounding the A atoms at the body-centered and corner positions differ by a 90° rotation about the z axis.

We summarize in Table II the A-A, A-B, and B-B bond lengths for RuO_2, OsO_2, and IrO_2. The lattice parameters a and c and position parameter u for RuO_2 and OsO_2 have been determined by Boman.[13] Though values of a and c for IrO_2 are available in the literature,[14] the position parameter u apparently has not been determined for this compound.

Each A atom has two B-atom neighbors at a distance $d_1 = \sqrt{2}ua$ and four at

$$d_2 = [2(\tfrac{1}{2} - u)^2 + (c/2a)^2]^{1/2} a \ .$$

All six of these A-B bond lengths are equal if the

TABLE II. Lattice parameters and bond lengths (Å) for the present AB_2 compounds with the rutile structure.

Type	(No.)	RuO_2	OsO_2	IrO_2
	a(Å)	4.4919	4.5003	4.4983
	c (Å)	3.1066	3.1839	3.1544
	c/a	0.696	0.708	0.701
	u	0.306	0.308	0.307[a]
	u^*	0.310	0.313	0.312
	$(c/a)_{\text{ideal}}$	0.586	0.586	0.586
	u_{ideal}	0.293	0.293	0.293
A-A	(2) $d_1 = c$	3.107	3.184	3.154
	(8) $d_2 = [\frac{1}{2} + (c/2a)^2]^{1/2}a$	3.536	3.558	3.550
	(4) $d_3 = a$	4.492	4.500	4.498
A-B	(2) $d_1 = \sqrt{2}\,ua$	1.944	1.960	1.953
	(4) $d_2 = [2(\frac{1}{2} - u)^2 + (c/2a)^2]^{1/2}a$	1.983	2.007	1.999
B-B	(1) $d_1 = \sqrt{2}\,(1 - 2u)a$	2.465	2.444	2.456
	(8) $d_2 = [\frac{1}{4} + (\frac{1}{2} - 2u)^2 + (c/2a)^2]^{1/2}a$	2.777	2.805	2.795
	(2) $d_3 = c$	3.107	3.184	3.154
	(2) $d_4 = [(1 - 2u)^2 + (2u)^2]^{1/2}a$	3.255	3.267	3.262

[a]Estimated value for u.

position parameter u has the special value, $u^* = \frac{1}{4}[1 + \frac{1}{2}(c/a)^2]$. The octahedral coordination of each A atom is ideal if $(c/a)_{\text{ideal}} = 2 - \sqrt{2}$ and $u_{\text{ideal}} = \frac{1}{2}(2 - \sqrt{2})$. In this case, the B-B bond lengths d_1, d_2, and d_3 of Table II are all equal. According to Table II, $u < u^*$ for both RuO_2 and OsO_2 by about 1.5% so that $d_1 < d_2$ by about 0.04 Å. We estimate u for IrO_2 by assuming that $u < u^*$ by a similar amount in this compound.

The space group forthe rutile structure is $D_{4h}^{14}(P4_2/mnm)$, which is nonsymmorphic. With the origin of coordinates at an A-atom site, the symmetry operations in this space group include two types. The first involve the symmetry operations $\{\alpha \mid \vec{R}_n\}$, where α is one of the eight point-group operations in D_{2h} and $\vec{R}_n$ is a general translation $\vec{R}_n = n_1\vec{t}_1 + n_2\vec{t}_2 + n_3\vec{t}_3$ with integer coefficients n_i. The second type of space-group operation has the form $\{\alpha' \mid \vec{R}_n + \vec{\tau}\}$, where α' spans the remaining eight point-group operations in D_{4h} (i.e., minus those in D_{2h}) and $\vec{\tau}$ is a nonprimitive translation,

$$\vec{\tau} = \tfrac{1}{2}(\vec{t}_1 + \vec{t}_2 + \vec{t}_3).$$

The point-group symmetries at the A-atom and B-atom sites are D_{2h} and C_{2v}, respectively. Since the irreducible representations for the D_{2h} point group include eight one-dimensional representations, one expects that the five A-atom d levels for an isolated AB_6 cluster with this symmetry would be split by the ligand field into five nondegenerate levels. Each of these ligand-field levels is doubly degenerate in a crystal with the rutile structure because of the presence of two A atoms per unit cell. These five doubly-degenerate ligand-field levels ultimately evolve into ten A-atom d bands when the effects of the lattice periodicity are taken into account.

Since each A atom is surrounded by a nearly octahedral array of six B atoms, it is convenient to represent its D_{2h} site symmetry as the sum of a large octahedral term plus a small orthorhombic distortion. As is well known, an octahedral ligand field causes a d level to be split into triply-degenerate t_{2g} and doubly-degenerate e_g components. For a regular octahedron with vertices along the coordinate axes, the symmetry of the t_{2g} orbitals is xy, yz, and zx while that of the e_g orbitals is $(3z^2 - r^2)$ and $(x^2 - y^2)$. The equivalent orbitals for the rutile structure, expressed in terms of the coordinate system of Fig. 1(a), are summarized in Table III. As indicated, the t_{2g} and e_g degeneracies are lifted by the orthorhombic distortion. In each case, the orbital combinations in Table III are such that they transform irreducibly under the D_{2h} point group. Since any linear combination of (xy) and $(3z^2 - r^2)$ orbitals satisfy this condition, the appropriate coefficients for *these* orbitals are determined by the octahedral component of the ligand field.

The C_{2v} symmetry at a B-atom site causes an analogous splitting of the oxygen $2p$ levels in these

TABLE III. Angular dependence of e_g and t_{2g} A-atom d orbitals $\varphi_\alpha(\vec{r} - \vec{r}_{Ai}) \equiv \alpha_i$ at sites $\vec{r}_{A1} = (0, 0, 0)$ and $\vec{r}_{A2} = (\frac{1}{2}, \frac{1}{2}, \frac{1}{2})$ of the rutile unit cell. The D_{2h} site symmetry is represented by a octahedral term plus an orthorhombic distortion.

	Orbitals		Point symmetry[a]	
Type	α_1	α_2	Octahedral	Orthorhombic
$(e_g)_1$	$-\frac{1}{2}[\sqrt{3}(xy)_1 + (3z^2 - r^2)_1]$	$\frac{1}{2}[\sqrt{3}(xy)_2 - (3z^2 - r^2)_2]$	Γ_{12}	N_1
$(e_g)_2$	$[(xy)_1 + (yz)_1]/\sqrt{2}$	$[(xz)_2 - (yz)_2]/\sqrt{2}$	Γ_{12}	N_3
$(t_{2g})_1$	$\frac{1}{2}[(xy)_1 - \sqrt{3}(3z^2 - r^2)_1]$	$-\frac{1}{2}[(xy)_2 + \sqrt{3}(3z^2 - r^2)_2]$	Γ'_{25}	N_1
$(t_{2g})_2$	$[(xz)_1 - (yz)_1]/\sqrt{2}$	$-[(xz)_2 + (yz)_2]/\sqrt{2}$	Γ'_{25}	N_2
$(t_{2g})_3$	$(x^2 - y^2)_1$	$-(x^2 - y^2)_2$	Γ'_{25}	N_4

[a]Notation is that of Ref. 15.

TABLE IV. Correspondence between the notation of Dimmock and Wheeler (DW) and Gay *et al.* (GAA) for the irreducible representations of the D_{4h}^{14} space group.

DW	GAA	DW	GAA	DW	GAA
Γ_1^+	Γ_1^+	M_1^+	M_1	Z_1	Z_1
Γ_2^+	Γ_2^+	M_2^+	M_2	Z_2	Z_3
Γ_3^+	Γ_3^+	M_3^+	M_3	Z_3	Z_4
Γ_4^+	Γ_4^+	M_4^+	M_4	Z_4	Z_2
Γ_5^+	Γ_5^-	M_5^+	M_9^-		
Γ_1^-	Γ_2^-	M_1^-	M_7	A_1	A_1
Γ_2^-	Γ_1^-	M_2^-	M_8	A_2	A_3
Γ_3^-	Γ_4^-	M_3^-	M_5	A_3	A_4
Γ_4^-	Γ_3^-	M_4^-	M_6	A_4	A_2
Γ_5^-	Γ_5^+	M_5^-	M_9^+		
X_1	X_1	R_1^+	R_1^+		
X_2	X_2	R_1^-	R_1^-		

rutile-type compounds. The proper combinations of p-type orbitals that transform irreducibly under the C_{2v} point group are $(x_i+y_i)/\sqrt{2}$, $(x_i-y_i)/\sqrt{2}$, and z_i; here, x_i, y_i, and z_i denote p-type orbitals localized at sites $\vec{r}_{B1}$, $\vec{r}_{B2}$, $\vec{r}_{B3}$, and $\vec{r}_{B4}$ $(i=1, \ldots, 4)$. The symmetry of the rutile structure is such that the orbitals $(x_i \pm y_i)/\sqrt{2}$ at sites $\vec{r}_{B1}$ and $\vec{r}_{B2}$ are equivalent to $(x_i \mp y_i)/\sqrt{2}$ at $\vec{r}_{B3}$ and $\vec{r}_{B4}$. The orbitals z_i transform according to the same representation at all four B-atom sites. The same is true for the B-atom s orbitals.

The irreducible representations for the D_{4h}^{14} space group have been worked out by Dimmock and Wheeler[16] and also by Gay *et al.*[17] In the present study, we shall employ the earlier notation of Dimmock and Wheeler. The relationship between this notation and that introduced by Gay *et al.* is presented in Table IV.

If Bloch sums are set up using properly symmetrized combinations of A-atom d orbitals and B-atom s-p orbitals, then one can apply standard group-theoretical methods to determine those irreducible representations of the D_{4h}^{14} space group that occur within a given subband at various symmetry points in the Brillouin zone. These results are summarized in Table V for the symmetry points Γ, X, M, Z, R, and A. Here, the A-atom d bands are subdivided only into their e_g and t_{2g} components (see Table III) and the B-atom p states into their (x, y) and z subbands. According to these results, we can immediately identify energy-band states with Γ_2^-, Γ_3^-, M_3^-, and M_4^- in terms of the B-atom z-type orbitals. Those with Γ_2^+, Γ_3^+, Z_2, M_3^+, M_4^+, and A_2 symmetry involve a covalent mixture of A-atom t_{2g} and B-atom (x, y) orbitals. The remaining states allow various combinations of hybridization and covalent mixing to occur.

B. APW calculations

The present APW calculations for rutile-type compounds apply many of the same general techniques that have been described in connection with

TABLE V. Number of times a given space-group representation occurs in a particular subband at various symmetry points in the Brillouin zone.

$\vec{k}$	A atom		B atom			$\vec{k}$	A atom		B atom		
	t_{2g}	e_g	s	x,y	z		t_{2g}	e_g	s	x,y	z
$\Gamma(0,0,0)$						$M(\frac{1}{2},\frac{1}{2},0)$					
Γ_1^+	1	1	1	1	···	M_1^+	1	1	1	1	···
Γ_2^+	1	···	···	1	···	M_2^+	1	1	1	1	···
Γ_3^+	1	···	···	1	···	M_3^+	1	···	···	1	···
Γ_4^+	1	1	1	1	···	M_4^+	1	···	···	1	···
Γ_5^+	1	1	···	···	1	M_5^+	1	1	···	···	1
Γ_1^-	···	···	···	···	···	M_1^-	···	···	···	···	···
Γ_2^-	···	···	···	···	1	M_2^-	···	···	···	···	···
Γ_3^-	···	···	···	···	1	M_3^-	···	···	···	···	1
Γ_4^-	···	···	···	···	···	M_4^-	···	···	···	···	1
Γ_5^-	···	···	1	2	···	M_5^-	···	···	1	2	···
$X(\frac{1}{2},0,0)$						$R(\frac{1}{2},0,\frac{1}{2})$					
X_1	2	1	2	4	···	R_1^+	3	2	1	2	1
X_2	1	1	···	···	2	R_1^-	···	···	1	2	1
$Z(0,0,\frac{1}{2})$						$A(\frac{1}{2},\frac{1}{2},\frac{1}{2})$					
Z_1	1	1	1	1	1	A_1	1	1	1	1	1
Z_2	1	···	···	1	···	A_2	1	···	···	1	···
Z_3	1	···	···	1	1	A_3	1	···	···	1	1
Z_4	···	1	1	1	···	A_4	···	1	1	1	···

TABLE VI. APW sphere radii and low-order Fourier coefficients $V_\Delta(\vec{K})$ for AB_2 compounds.

		RuO_2	OsO_2	IrO_2
	R_A (a.u.)	2.02	2.04	2.03
	R_B (a.u.)	1.65	1.66	1.66
$\vec{K} \equiv (\xi, \eta, \zeta)$	$\exp(i\vec{K}\cdot\vec{\tau})$		$V_\Delta(\vec{K})$ (Ry)	
(0,0,0)	+1	−1.1848	−1.2025	−1.1822
(1,0,0)	−1	0	0	0
(1,1,0)	+1	−0.0907	−0.0933	−0.0928
(0,0,1)	−1	0	0	0
(1,0,1)	+1	−0.0014	−0.0039	−0.0032
(2,0,0)	+1	0.0342	0.0350	0.0344
(1,1,1)	−1	−0.0204	−0.0210	−0.0205
(2,1,0)	−1	0.0064	0.0065	0.0069
(2,0,1)	−1	0	0	0
(2,1,1)	+1	0.0224	0.0250	0.0245
(2,2,0)	+1	0.0340	0.0378	0.0372
(0,0,2)	+1	0.0274	0.0262	0.0285
(3,0,0)	−1	0	0	0

similar calculations for compounds with the ReO_3,[18] rocksalt,[19] perovskite,[20] and layer[21] structures. The approximate crystal potentials are calculated by overlapping the atomic Hartree-Fock-Slater charge densities of Herman and Skillman.[22] Exchange is treated by Slater's original free-electron exchange approximation.[23] The assumed electronic configurations of the transition-metal and oxygen atoms are $d^n s^2$ and s^2p^4, respectively.

Since the rutile structure is relatively loose packed in terms of nonoverlapping atomic spheres, the corrections to the muffin-tin potential $V_\Delta(\vec{r})$ in the region between the APW spheres have an important effect on the energy-band results. These have been included in each of the earlier APW calculations[18-21] by adding the appropriate Fourier coefficient $V_\Delta(\vec{K})$ to the standard muffin-tin APW matrix elements. Each of these calculations neglects the nonspherical corrections to the muffin-tin potential inside the APW spheres.

The values for the transition-metal and oxygen APW sphere radii assumed in the present calculations are listed in Table VI. These radii are chosen so that the metal and oxygen spheres touch along the shortest metal-oxygen bond distance (d_1 in Table II). In addition, the ratio $R_A/R_B \approx \frac{7}{6}$ is assumed so as to equalize the relative convergence of the metal d and oxygen $2p$ states and minimize the corrections to the muffin-tin potential within and between the APW spheres.[18-21]

With these values for the sphere radii, about 66% of the unit cell lies outside the APW spheres. In this respect, the rutile structure is intermediate to that of[18] ReO_3 (76%) and the layer compounds[21] (62%). The corrections to the muffin-tin potential in the region between the APW spheres $V_\Delta(\vec{r})$ have very similar magnitudes in RuO_2, OsO_2, and IrO_2; they range from −1.3 to +0.6 Ry relative to the muffin-tin constant. The nonspherical corrections just inside the metal and oxygen APW spheres exhibit peak-to-peak variations of about 0.4–0.5 Ry.

The Fourier coefficients $V_\Delta(\vec{K})$ are determined by direct summation:

$$V_\Delta(\vec{K}) = N^{-1} \sum_n e^{i\vec{K}\cdot\vec{r}_n} V_\Delta(\vec{r}_n) , \tag{5}$$

where N spans a total of 11 520 uniformly distributed points in the tetragonal unit cell. The muffin-tin corrections $V_\Delta(\vec{r}_n)$ are set equal to zero for all $\vec{r}_n$ within any of the APW spheres. The values for the lowest-order $V_\Delta(\vec{K})$'s for the present rutile-type compounds are included in Table VI. Because of the nonsymmorphic nature of the D_{4h}^{14} space group, many of the $V_\Delta(\vec{K})$ vanish or alternate in sign for different wave vectors in the star of $\vec{K}$ when $\exp(i\vec{K}\cdot\vec{\tau}) = -1$. For this class of wave vectors, it is readily shown that $V_\Delta(\vec{K}) = 0$ if either ξ or $\eta = 0$. This is a special case of the general result that $V_\Delta(\vec{K}) = V_\Delta(\alpha\vec{K}) = -V_\Delta(\alpha'\vec{K})$ for the point-group operations α and α' defined in Sec. II A.

APW calculations have been performed for RuO_2 at the zone center Γ to determine the effect of the muffin-tin corrections $V_\Delta(\vec{r})$ on energy eigenvalues of the valence and conduction bands. It is found that muffin-tin energy levels are shifted by as much as 0.12 Ry when these corrections are included. The average shifts are in the range 0.04–0.06 Ry. These shifts are intermediate to those found earlier in similar calculations for [18]ReO_3 (0.25 Ry) and the layer compounds[21] (0.08 Ry), indicating that the fraction of the unit cell volume outside the APW spheres is the principal factor that determines the importance of these corrections.

Since the rutile structure has inversion symmetry, the APW matrix elements can be set up so that they are real rather than complex. Some exceptions involve the time-reversal-degenerate states on the surface of the Brillouin zone, such as $M_1 \pm M_2 \pm$ and $M_3 \pm M_4 \pm$. The symmetrized APW matrix for these states can be kept real if a subgroup of the full group of the wave vector is utilized in the calculations for these states. When this is done, the determinant of the APW matrix no longer changes sign as a function of energy but instead approaches zero quadratically near each doubly-degenerate energy eigenvalue. Similar situations occur along symmetry lines on the surface of the Brillouin zone.

Convergence studies indicate that roughly 280 APW basis functions are required in order to reduce convergence errors to about 0.002 Ry. The wave vectors $(\vec{k}+\vec{K})$ for these APW's include all those for which $(\vec{k}+\vec{K})^2$ is less than about 11.5 Ry. This leads to symmetrized APW matrices with dimensions as large as 85×85 for calculations at the

symmetry points Γ, X, M, Z, R, and A in the Brillouin zone.

Preliminary APW calculations were carried out for RuO_2 using less accurate values for the lattice parameters a and c and the position parameter u for this compound.[24] The results of these preliminary calculations have been applied by Graebner, *et al.*[7] in the preceding paper as a basis for interpreting their magnetothermal-oscillation data for RuO_2, OsO_2, and IrO_2. They found that it was necessary to adjust empirically the relative energies of several critical conduction-band states in order to obtain Fermi-surface topologies that were consistent with their data. As we shall show in the following sections, the present calculations for RuO_2, which involve Boman's[13] more accurate values for a, c, and u, yield results that are in better agreement with experiment than those obtained in this preliminary study. It is believed that accurate values for the position parameter u are particularly critical in this respect since it represents an important factor in determining the metal-oxygen bond lengths in the rutile structure. This preliminary band calculation for RuO_2 involved a value for u (0.31) that was slightly greater than u^* (0.309); as a result, the Ru-O bond length $d_2 < d_1$, whereas $d_2 > d_1$ in Table II.

C. LCAO model

The LCAO interpolation model that is applied to fit the APW results for RuO_2, OsO_2, and IrO_2 involves a total of 26 basis functions. These include ten Bloch sums formed from the metal-atom d orbitals, four from the oxygen $2s$ orbitals, and twelve from the oxygen $2p$ orbitals. This model omits the unoccupied conduction-band states that evolve from the metal-atom s-p orbitals. The results of the APW calculations described in Sec. II B reveal that the bottom of these metal-atom s-p bands occurs slightly above the d bands in each compound. The energy separation between the top of the d band and the bottom of this s-p band is 0.18, 0.07, and 0.15 Ry in RuO_2, OsO_2, and IrO_2, respectively.

The application of the Slater-Koster LCAO interpolation method to the rutile structure is complicated by the low symmetry of this structure. It is clear from Fig. 1 and Table II that bond distances and bond directions generally depend both on the c/a ratio and the position parameter u. Unlike the situation in most cubic crystals,[10] many of the nearest-neighbor bonds occur along low-symmetry directions in the rutile structure. As Egorov *et al.*[25] have shown, this leads to a large number of independent Slater-Koster energy parameters $E_{\alpha,\beta}(\vec{r}_i)$.

Another difficulty in applying the LCAO method to the rutile structure concerns the choice of a suitable coordinate system. The natural coordinate system for describing the translational symmetry of the lattice is that shown in Fig. 1(a). However, as discussed in Sec. II A, the orbitals at the metal-atom and oxygen sites are more simply described in terms of local coordinate systems that are rotated by $\pm\frac{1}{4}\pi$. After considering these alternatives, it was decided that the coordinate system in Fig. 1(a) was the more convenient one for setting up the LCAO method for the rutile structure.

Mitra *et al.* [26] have worked out the LCAO matrix for the rutile structure in terms of this same coordinate system. They reduce all energy integrals $E_{\alpha,\beta}(\vec{r}_i)$ to the two-center approximation.[10] In general, their expressions for these matrix elements appear to be equivalent to those derived during the course of the present investigation. Mitra *et al.* include the metal-atom s-p orbitals in their LCAO basis so that the dimension of their model Hamiltonian is 34×34.

There are several minor differences between the present LCAO model and that of Mitra *et al.* They assume that their Bloch sums are formed from orthogonalized atomic orbitals so that their overlap matrix is diagonal. The present model allows orbital overlap between the metal-atom d and the oxygen s-p orbitals. As discussed previously,[18-20] this not only improves the accuracy of the LCAO fit, but it also treats ligand-field effects in a realistic manner. All of the LCAO matrix elements of Mitra *et al.* are complex, except those involving metal-metal interactions. However, both the energy and overlap matrices can be made real by applying a simple unitary transformation involving pairs of oxygen $2s$ and $2p$ orbitals at sites $\vec{r}_{B1}$ and $\vec{r}_{B2}$ as well as $\vec{r}_{B3}$ and $\vec{r}_{B4}$.

One difficulty with the LCAO formulation of Mitra *et al.* involves the parametrization of the d-orbital energies. Slater and Koster[10] propose a common d-orbital energy d_0 for both the e_g and t_{2g} subbands in the two-center approximation for cubic structures. Actually, these energies can be different in the two-center approximation since they involve a sum of two-center integrals, each of which contains an orbital charge density at the origin and a potential at a neighboring site. Mitra *et al.* incorrectly assign the t_{2g} orbital-energy parameter to the xy, yz, and zx basis functions and an e_g energy to those with (x^2-y^2) and $(3z^2-r^2)$ symmetry. As shown in Table III, the approximate separation of the metal-atom d orbitals into e_g and t_{2g} states involves linear combinations of these orbitals.

According to the analysis of Egorov *et al.*,[25] there are five independent d-orbital energy parameters in the rutile structure, one for each pair of orbitals in Table III. In addition, there are three independent oxygen $2p$ orbital energies and one for

the oxygen $2s$ states. The energy parameters for the $2p$ orbitals $(x_i+y_i)/\sqrt{2}$, $(x_i-y_i)/\sqrt{2}$, and z_i at sites $\vec{r}_{B1}$ and $\vec{r}_{B2}$ are equivalent to those for $(x_i-y_i)/\sqrt{2}$, $(x_i+y_i)/\sqrt{2}$, and z_i at sites $\vec{r}_{B3}$ and $\vec{r}_{B4}$, respectively. Thus, the orbital energy is nondiagonal in the present coordinate system. The detailed form of the diagonal and off-diagonal matrix elements is readily determined by the condition that this submatrix be reduced to diagonal form by the appropriate unitary transformation that is indicated above for $2p$ orbitals and in Table III for the metal-atom d orbitals.

The present LCAO model has been set up to include five independent metal-atom d-orbital energies $(E_{d1}-E_{d5})$, three oxygen $2p$-orbital energies (E_{x+y}, E_{x-y}, E_z at sites $\vec{r}_{B1}$ or $\vec{r}_{B2}$), and an oxygen $2s$ energy (E_s). Metal-metal d-d, metal-oxygen d-s and d-p, and oxygen-oxygen s-s and p-p interactions are treated in the two-center approximation and span the bond distances included in Table II. The d-d interactions between the first three shells of A-A neighbors in Table II involve nine two-center integrals, $(dd\sigma)_i$, $(dd\pi)_i$, and $(dd\delta)_i$, where $i=1$, 2, 3 denote the A-A bond distances d_1, d_2, d_3. The oxygen-metal s-d and p-d covalency-overlap interactions involve twelve parameters, $(sd\sigma)_i$, $(S_s)_i$, $(pd\sigma)_i$, $(S_\sigma)_i$, $(pd\pi)_i$, $(S_\pi)_i$, with $i=1$, 2. The oxygen s-s and p-p interactions span four shells of neighbors and involve twelve parameters, $(ss\sigma)_i$, $(pp\sigma)_i$, $(pp\pi)_i$, with $i=1,\ldots,4$. The hybridization matrix elements in the oxygen s-p block are set equal to zero in this model. In all, this LCAO model contains a total of 42 parameters that are to be determined by fitting the APW results at symmetry points in the Brillouin zone.

The first step in determining these LCAO parameters requires the reduction of the full 26×26 LCAO matrix into its noninteracting subblocks at those symmetry points in the Brillouin zone where the APW results are to be fit. This assures that each APW eigenvalue is fit by an LCAO function with the proper symmetry. The dimensions of a given submatrix at Γ, X, M, Z, R, or A are obtained by summing the entries in a single row in Table V. The dimensions of these submatrices range from 1×1 (Γ_{2^-}, Γ_{3^-}, M_{3^-}, M_{4^-}) to 9×9 (X_1, R_{1^+}). Summing over all entries, we find that there are a total of 92 APW-LCAO eigenvalues involved.

By means of a nonlinear-least-squares fitting procedure,[19] unique values for these 42 LCAO parameters are determined from the 92 APW eigenvalues. Even with relatively crude starting values, this method usually converges within 10–15 iterations. It was found that some LCAO parameters provided little to no improvement in the accuracy of the over-all LCAO fit to the APW results. This led to the elimination of five LCAO parameters, thereby reducing their total number to 37. For example, it was found that a single d-orbital energy E_d was adequate for treating all five metal-atom d subbands. In addition, these tests showed that $(ss\sigma)_4$ could be neglected. The final values of these 37 LCAO parameters for RuO_2, OsO_2, and IrO_2 are contained in Table VII.

TABLE VII. LCAO parameters for RuO_2, OsO_2, and IrO_2. APW eigenvalues [relative to the muffin-tin constant $V_\Delta(0)$] are shifted by Δ so that the top of the $2p$ band $E(\Gamma_{3^+})=0$.

Param.	RuO_2	OsO_2	IrO_2	Param.	RuO_2	OsO_2	IrO_2
E_s	−1.1887	−1.1757	−1.1862	$(dd\sigma)_2$	−0.0095	−0.0145	−0.0104
$(ss\sigma)_1$	−0.0181	−0.0187	−0.0188	$(dd\pi)_2$	0.0003	0.0007	−0.0003
$(ss\sigma)_2$	−0.0083	−0.0084	−0.0081	$(dd\delta)_2$	0.0002	0.0010	0.0010
$(ss\sigma)_3$	−0.0057	−0.0059	−0.0056	$(dd\sigma)_3$	0.0073	0.0076	0.0083
E_{x+y}	−0.0747	−0.0723	−0.0744	$(dd\pi)_3$	0.0018	0.0022	0.0022
E_{x-y}	−0.0980	−0.0832	−0.0945	$(dd\delta)_3$	−0.0028	−0.0032	−0.0032
E_z	−0.0906	−0.0787	−0.0895	$(sd\sigma)_1$	−0.1633	−0.1896	−0.1717
$(pp\sigma)_1$	0.0466	0.0484	0.0464	$(S_s)_1$	0.0361	0.0453	0.0392
$(pp\pi)_1$	−0.0161	−0.0174	−0.0155	$(pd\sigma)_1$	−0.1849	−0.2008	−0.1966
$(pp\sigma)_2$	0.0290	0.0272	0.0291	$(S_\sigma)_1$	0.0838	0.0925	0.0915
$(pp\pi)_2$	−0.0056	−0.0058	−0.0059	$(pd\pi)_1$	0.0816	0.0884	0.0862
$(pp\sigma)_3$	0.0181	0.0171	0.0177	$(S_\pi)_1$	−0.0848	−0.0924	−0.0958
$(pp\pi)_3$	−0.0001	−0.0001	0.0003	$(sd\sigma)_2$	−0.1837	−0.2016	−0.1917
$(pp\sigma)_4$	0.0159	0.0156	0.0167	$(S_s)_2$	0.0590	0.0655	0.0634
$(pp\pi)_4$	−0.0006	−0.0005	−0.0003	$(pd\sigma)_2$	−0.1638	−0.1766	−0.1733
E_d	0.1591	0.2126	0.1094	$(S_\sigma)_2$	0.0748	0.0846	0.0804
$(dd\sigma)_1$	−0.0366	−0.0409	−0.0353	$(pd\pi)_2$	0.0722	0.0772	0.0747
$(dd\pi)_1$	0.0039	0.0058	0.0036	$(S_\pi)_2$	−0.0136	−0.0212	−0.0149
$(dd\delta)_1$	0.0019	0.0023	0.0022	ξ_d	0.0110	0.0300	0.0330
				Δ	−0.0684	−0.0704	−0.0688
rms error	0.0048	0.0052	0.0054	max. error	0.0129	0.0170	0.0168

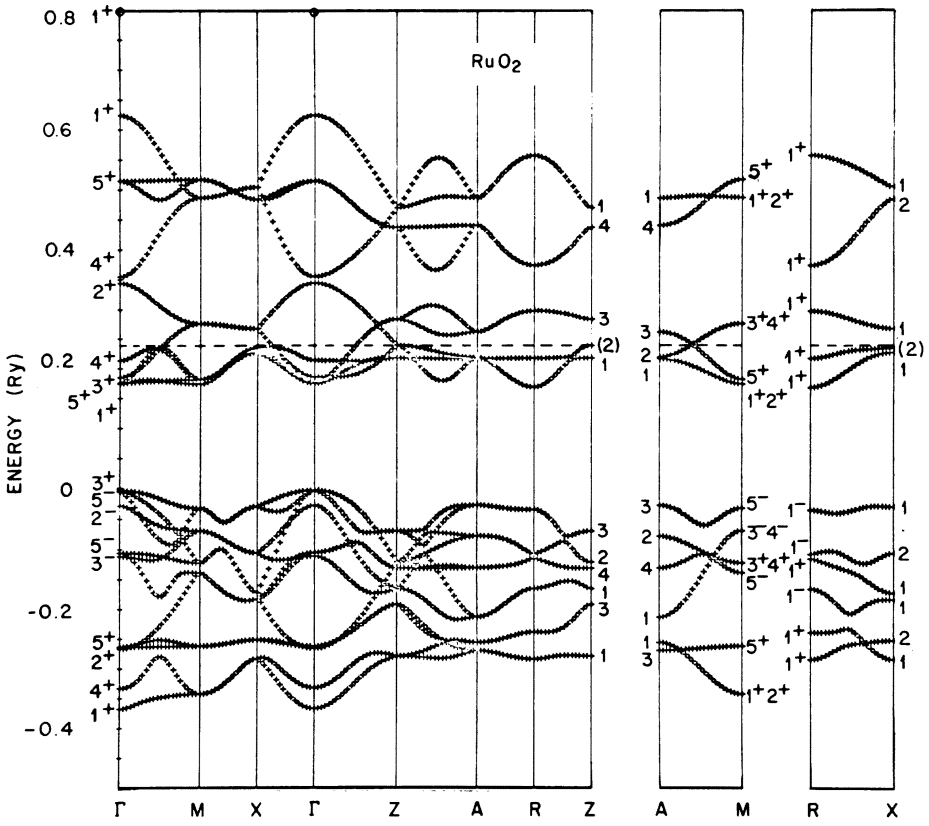

FIG. 2. APW-LCAO energy bands for RuO_2.

In determining the LCAO parameters in Table VII, some of the critical energy-band states near the Fermi energy E_F in RuO_2 and OsO_2 (X_2, Z_2) and IrO_2 (X_1, M_{3^+}, M_{4^+}, Z_3, R_{1^+}, A_3) were weighted more heavily in the fitting procedure. This slight trimming up of the bands near E_F had virtually no effect on the over-all quality of the LCAO fit. In fact, the difference in the rms error between the weighted and unweighted LCAO fits was always less than 10^{-4} Ry.

Caruthers *et al.*[11] have applied the Slater-Koster LCAO interpolation method to fit the results of their APW calculations for VO_2 at the Γ, Z, and A points in the Brillouin zone. Their LCAO basis is somewhat different from that involved in the present model. For example, it includes Bloch sums formed from excited oxygen $3s$ and $3d$ (with xz and yz symmetry) orbitals but omits the occupied oxygen $2s$ states. At the vanadium sites, they include Bloch sums formed from both the $3d$ and $4s$ orbitals. This leads to a 36×36 complex LCAO matrix. Their LCAO model fits 42 APW energy eigenvalues and wave functions in terms of 43 parameters with an 0.02-Ry rms error. By comparison, the present LCAO model fits 92 APW eigenvalues by means of 37 parameters with an 0.005-Ry rms error.

Since the present LCAO model is applied to fit APW results only at six symmetry points in the Brillouin zone, there is perhaps some question concerning its accuracy at intermediate points along symmetry lines and at general points in the Brillouin zone. A detailed study of this problem was carried out using the results of the preliminary APW calculations for RuO_2 that are described in the preceding section. In this study, the LCAO fit was extended to include 92 additional APW energy eigenvalues at the midpoints of the Λ, Σ, S, and V lines in Fig. 1(b). It was found that this produced no change in the rms error and negligible changes in the values of the LCAO parameters.

Finally, the present LCAO model has been generalized to include the effects of spin orbit coupling for the metal-atom d orbitals. This requires the addition of a final parameter ξ_d that is listed in Table VII. Spin-orbit coupling doubles the size of the LCAO matrix and causes it to become complex. However, as shown in Secs. III–V, spin-orbit coupling produces important changes in the Fermi-surface topologies for each of these compounds.

III. RESULTS

The APW-LCAO energy-band results for RuO_2, OsO_2, and IrO_2 are plotted in Figs. 2–4, respectively. In each compound, the zero of energy co-

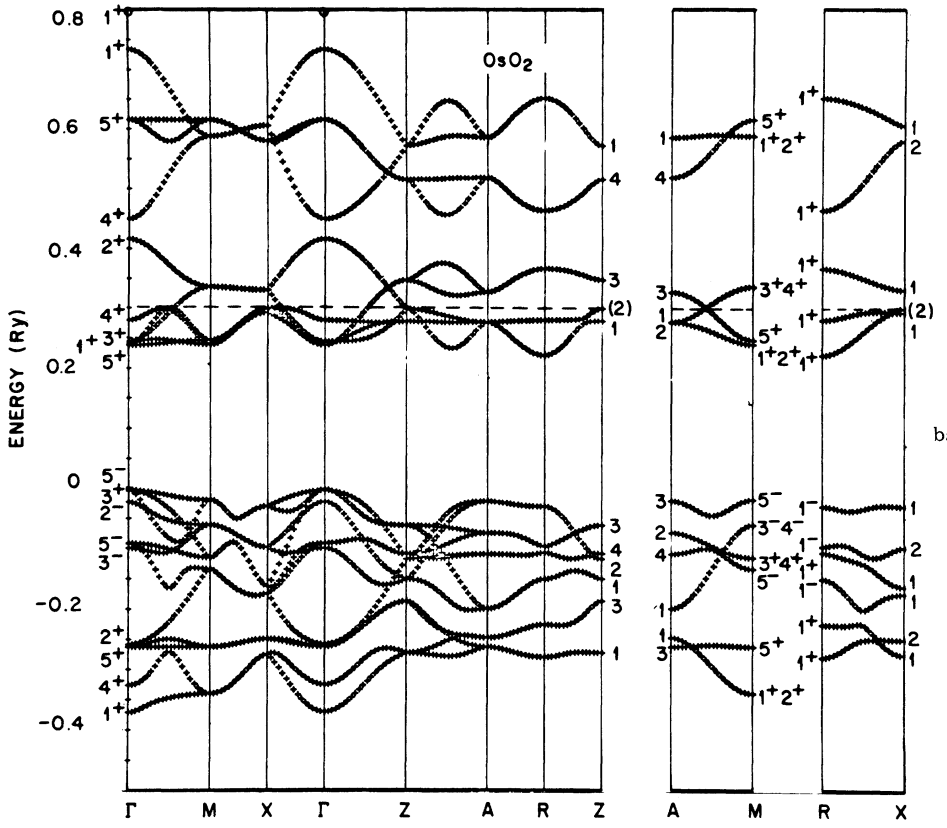

FIG. 3. APW-LCAO energy bands for OsO_2.

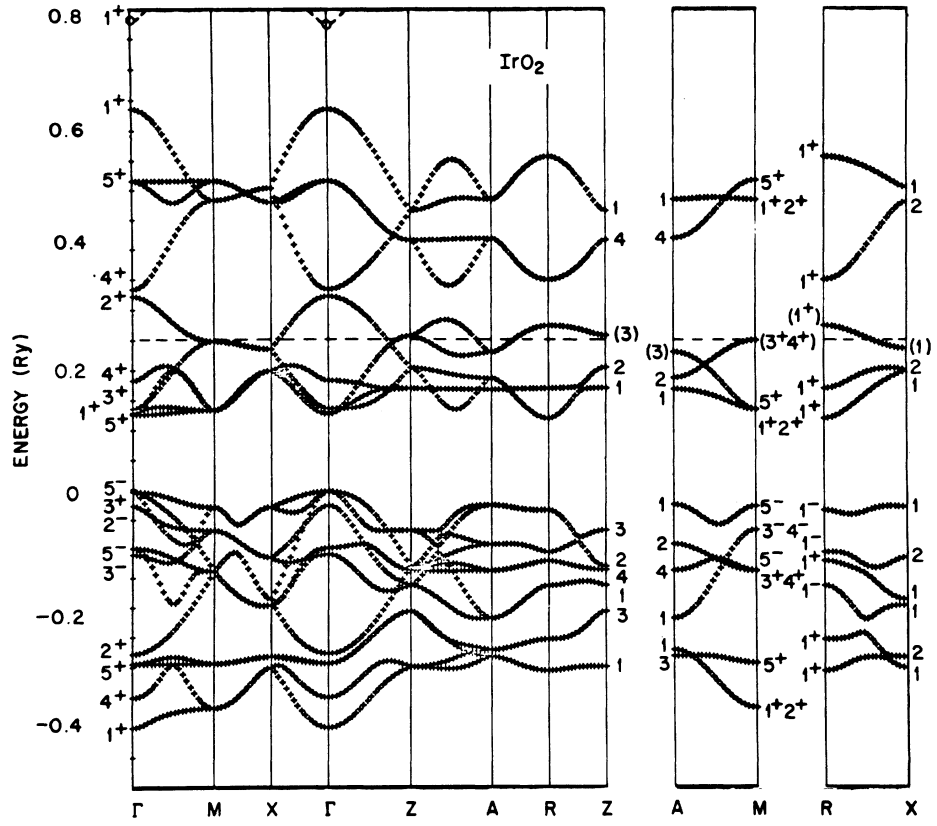

FIG. 4. APW-LCAO energy bands for IrO_2.

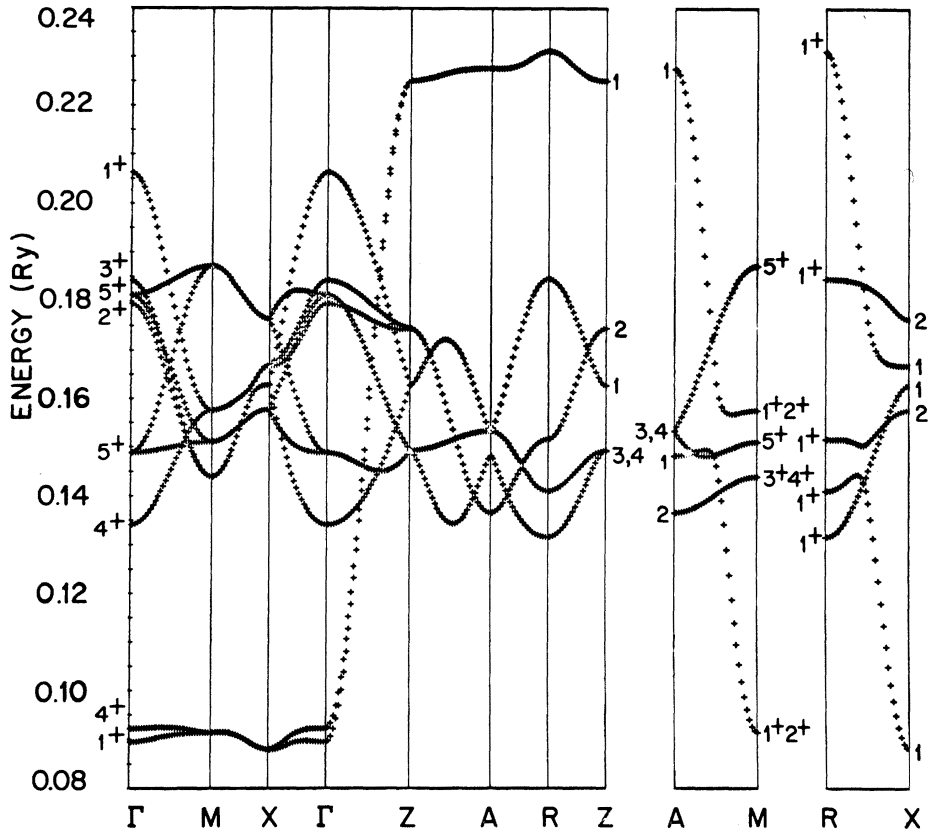

FIG. 5. Ruthenium 4*d* bands obtained by setting Ru-O overlap-covalency LCAO parameters equal to zero.

incides with that state (Γ_{3^+}) which forms the top of the oxygen 2*p* bands. The value of $E(\Gamma_{3^+})$ relative to the muffin-tin constant for each compound is equal to $-\Delta$ in Table VII. Above the 12 oxygen 2*p* bands are the 10 metal-atom *d* bands. These are separated into an upper fourfold-degenerate e_g manifold and a lower sixfold-degenerate t_{2g} subband. The Fermi energy E_F, which is indicated by the dashed horizontal line, falls in the midst of the t_{2g}-band complex in each compound. Those states near E_F which have been weighted more heavily in the LCAO fitting procedure of Sec. IIC are enclosed within parentheses. Though not shown here, the four oxygen 2*s* bands have a width of about 0.1 Ry and are centered at -1.22 Ry for each compound in terms of the energy scales of Figs. 2–4.

The Γ_{1^+} state near the top of each of these figures represents the bottom of the metal-atom *s*-*p* bands. It is well known that these *s*-*p* bands overlap and hybridize with the *d* bands in a typical transition metal. However, in the case of the transition-metal oxides, these metal-atom *s*-*p* orbitals are subject to strong overlap-covalency interactions with the oxygen 2*s*-2*p* orbitals which raise their energy so that they lie well above the *d* bands.[18–20] A similar situation is also found in the transition-metal dichalcogenides with layer-type structures.[21] Since the present LCAO model does not include the metal-atom *s*-*p* orbitals, these effects are treated implicitly rather than explicitly in our model by means of "effective" tight-binding parameters.

The importance of metal-oxygen covalency-overlap interactions in determining both the width and topology of the valence and conduction bands is illustrated in Fig. 5, where all metal-oxygen overlap-covalency parameters for RuO_2 are set equal to zero. These results demonstrate that most of the width of the "antibonding" *d* bands arises from the covalency-overlap interactions with the oxygen 2*s*-2*p* bands. This over-all picture is analogous to one that has been described previously in connection with the ReO_3 band structure.[18] In this limit, one would also expect a significant decrease in the energy of the metal *s*-*p* bands to an extent that they would overlap the *d* bands.

The energy-band results of Fig. 5 exhibit several features that are worth noting. First, it is found that the effect of setting overlap-covalency interactions equal to zero alters the energies of the "antibonding" *d* states to a greater degree than those of the "bonding" *s*-*p* bands. Whereas the oxygen 2*p*-band width is reduced by 38%, the ruthenium *d*-band width is decreased by 70% in this

approximation. This asymmetry between bonding and antibonding states is the key reason for including orbital-overlap effects explicitly in our LCAO model.

Another interesting feature of these results in Fig. 5 is the presence of a pair of nearly two-dimensional bands that are relatively flat in the $\Gamma MX(\zeta=0)$, $ZAR(\zeta=\frac{1}{2})$, as well as intermediate planes of the Brillouin zone. These bands evolve from the $(3z^2-r^2)$-type orbitals at sites $\vec{r}_{A1}$ and $\vec{r}_{A2}$, respectively. The LCAO matrix elements for these orbitals contain nearest-neighbor d-d interactions along the c axis involving the large $(dd\sigma)_1$ parameters of Table VII. As a result, $E(\vec{k})$ for these states is approximately $E_d+2(dd\sigma)_1\cos 2\pi\zeta$. This represents a total bandwidth of $4|(dd\sigma)_1|$ for this subband, which corresponds to about 0.14 Ry in RuO_2.

At first sight, the flat bands in the ZAR planes of Figs. 2–4 just below E_F appear to be a vestige of these one-dimensional $(3z^2-r^2)$-type subbands. A detailed study shows that these bands are very nearly flat throughout the entire ZAR plane. The LCAO wave functions for these states reveal that they involve almost exclusively the $(t_{2g})_1$ orbital combinations $\frac{1}{2}[(xy)_1-\sqrt{3}(3z^2-r^2)_1]$ and $\frac{1}{2}[-(xy)_2-\sqrt{3}(3z^2-r^2)_2]$ of Table III. Thus, we conclude that this flat band represents a ligand-field level for which the s-d and p-d overlap-covalency interactions are very nearly zero throughout the entire $ZAR(k_z=\pi/c)$ plane. The opposite is true for the $(e_g)_1$ orbital combinations $\frac{1}{2}[-\sqrt{3}(xy)_1-(3z^2-r^2)_1]$ and $\frac{1}{2}[\sqrt{3}(xy)_2-(3z^2-r^2)_2]$ of Table III, which interact strongly with the oxygen $2s$-$2p$ states, thus raising their energy by about 0.4 Ry. The net effect of similar interactions involving the remaining e_g and t_{2g} orbital combinations of Table III is to produce nonoverlapping e_g and t_{2g} subbands in each of these compounds.

We can achieve a more detailed identification of the various t_{2g} subbands in terms of these orbital combinations. For example, the $(t_{2g})_1$ subband involves the states Γ_{1+}, Γ_{4+}, X_1, M_{1+}, M_{2+}, Z_1, A_1, R_{1+} at symmetry points in the zone while the $(t_{2g})_2$ and $(t_{2g})_3$ subbands represent the combinations Γ_{5+}, X_2, M_{5+}, Z_3, A_3, R_{1+} and Γ_{2+}, Γ_{3+}, X_1, M_{3+}, M_{4+}, Z_2, A_2, R_{1+}, respectively. This identification of the t_{2g} subbands allows a more precise description of the conduction bands in Figs. 2–4. For example, the $(t_{2g})_1$ subband is below E_F and almost completely occupied in all three compounds. In the d^4 compounds RuO_2 and OsO_2, the $(t_{2g})_2$ subband is below E_F in the ΓMX $(k_z=0)$ plane and above E_F in the ZAR $(k_z=\pi/c)$ plane, while the $(t_{2g})_3$ subband is partially occupied in ΓMX plane and (almost) fully occupied in the ZAR plane. The above qualification refers to RuO_2, where the band with Z_2 symmetry is slightly above E_F. In the case of IrO_2, the Fermi surface is determined by the partially filled $(t_{2g})_2$ subbands in the $k_z=0$ and $k_z=\pi/c$ planes, respectively.

The presence of three independent t_{2g} subbands in the rutile structure suggests that the Fermi-surface topology in each compound will depend critically on the relative position of each subband relative to E_F. As a result, we can anticipate more difficulty in obtaining accurate Fermi-surface predictions in these rutile-type compounds than in a cubic compound such as ReO_3, where all three t_{2g} subbands are equivalent.[18]

The results shown in Fig. 6 illustrate the effect of spin-orbit coupling on the metal-atom d states in RuO_2, OsO_2, and IrO_2. The values of the spin-orbit parameter ξ_d are listed in Table VII. The value of ξ_d for ruthenium is the atomic value of Herman and Skillman.[22] The corresponding values for OsO_2 and IrO_2 are 20% smaller than the Herman-Skillman values. This adjustment was introduced in order to improve the over-all agreement between the calculated Fermi-surface dimensions and topology and that obtained empirically by Graebner *et al.*[7]

Spin-orbit coupling causes important changes in the band structure near E_F in each of these compounds. In the d^4 compounds RuO_2 and OsO_2, these changes are particularly important in the $\{110\}$ symmetry planes where states that are even and odd under reflection frequently cross one another when $\xi_d=0$. These crossings are removed by the effects of spin-orbit coupling. A similar change occurs along the AM or V symmetry line, where an accidental degeneracy involving doubly-degenerate (excluding spin) states V_3V_4 and V_5 is removed. In the case of IrO_2, the important effects of spin-orbit coupling occur on the $\{100\}$ surface of the Brillouin zone where all bands are doubly-degenerate (excluding spin) when $\xi_d=0$. This degeneracy is removed in the relativistic limit, except along the $MX(Y)$ and $MA(V)$ symmetry lines, where a twofold degeneracy persists. We also note that spin-orbit coupling splits and broadens the flat ligand-field levels that are found in the ZAR plane of Figs. 2–4.

The present APW-LCAO band model has been applied to calculate the density-of-states curves for RuO_2, OsO_2, and IrO_2. The results of these calculations are presented in Figs. 7–9. The curves for $\xi_d=0$ are determined by sampling $E(\vec{k})$ at nearly 70 000 uniformly distributed points in the Brillouin zone. The sampling is reduced to 12 000 points for the calculations involving spin-orbit coupling. A comparison of the density-of-states curves in the energy range of the oxygen $2s$-$2p$ bands indicates that either calculation includes an adequate sampling of states. In general, the density-of-states curves for each of these compounds

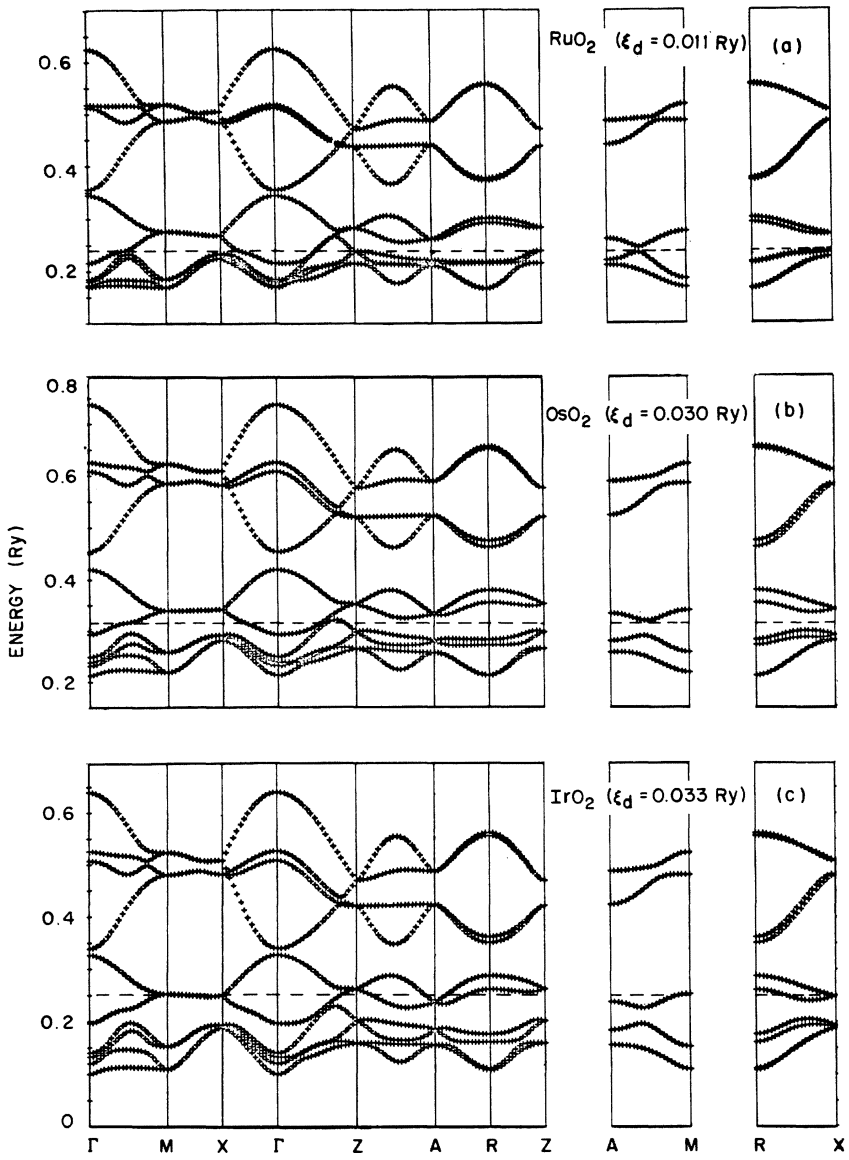

FIG. 6. Metal-atom d bands including spin-orbit coupling for (a) RuO_2; (b) OsO_2; (c) IrO_2.

are quite similar. In the energy range of the d bands, this is only true when $\xi_d = 0$. In this case, the flat doubly-degenerate band in the ZAR plane produces a huge narrow peak in the density-of-states $N(E)$ slightly below the Fermi energy. This peak is largely washed out by the effects of spin-orbit coupling, particularly in the case of the $5d$ compounds OsO_2 and IrO_2.

The intersection of the calculated Fermi surfaces of these compounds with the symmetry planes of the Brillouin zone is shown in the first two columns in Fig. 10. The results in the first column are obtained in the nonrelativistic limit where $\xi_d = 0$. The Fermi surfaces for the d^4 compounds RuO_2 and OsO_2 consist primarily of equal numbers of holes in the 4th (d-type) band (h_4) and electrons in the 5th band (e_5). Small hole pockets (h_3) occur near Z and along the $AM(V)$ line in RuO_2; the former are absent in OsO_2. As shown in the second column, spin-orbit coupling pinches off these protrusions of the d^4 Fermi surfaces in the $\{110\}$ plane and greatly simplifies their topologies. The Fermi surface for the d^5 compound IrO_2 contains equal numbers of holes in the fifth band (h_5) and electrons in the sixth band (e_6). As shown in the center, spin-orbit coupling significantly alters the topology of these various sheets as well.

IV. COMPARISON WITH EXPERIMENT

Unfortnunately, all of the experimental studies on RuO_2, OsO_2, and IrO_2 have probed their electronic properties in the immediate vicinity of the

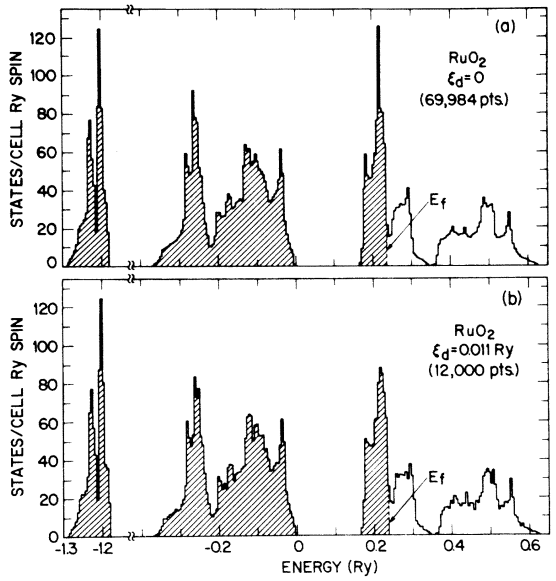

FIG. 7. $N(E)$ curves for RuO_2 with (a) $\xi_{4d}=0$; (b) $\xi_{4d}=0.011$ Ry.

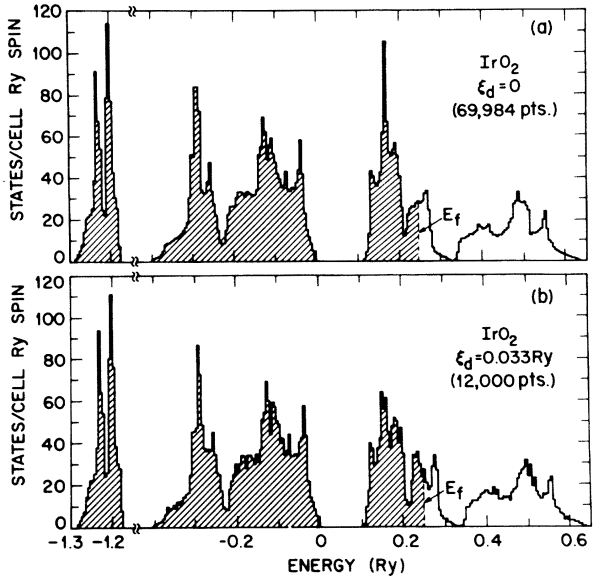

FIG. 9. $N(E)$ curves for IrO_2 with (a) $\xi_{5d}=0$; (b) $\xi_{5d}=0.033$ Ry.

Fermi energy E_F. At the present time, there exist no optical or photoemission data to help pin down the least reliable feature of the present energy-band results, namely, the energy separation between the metal-atom d and the oxygen $2s$-$2p$ bands. A common feature of most energy-band calculations for transition-metal oxides[11,18-20] is the fact that approximate crystal potentials of the type used here tend to overestimate the p-d energy separation by several eV. Therefore, it is expectec that similar errors may exist in the present results for RuO_2, OsO_2, and IrO_2. Such errors could possibly affect the details of the energy bands near E_F since, as shown in Fig. 5, these are largely determined by the effects of metal-oxygen overlap-covalency interactions. In terms of second-order perturbation theory, the strength of these interactions is inversely proportional to the energy denominators $(E_d - E_s)$ and $(E_d - E_p)$. One advantage of the present APW-LCAO approach is the fact that it allows one to compensate for these errors by adjusting a single LCAO parameter (E_d) in those cases where the s-d or p-d separation is known experimentally.

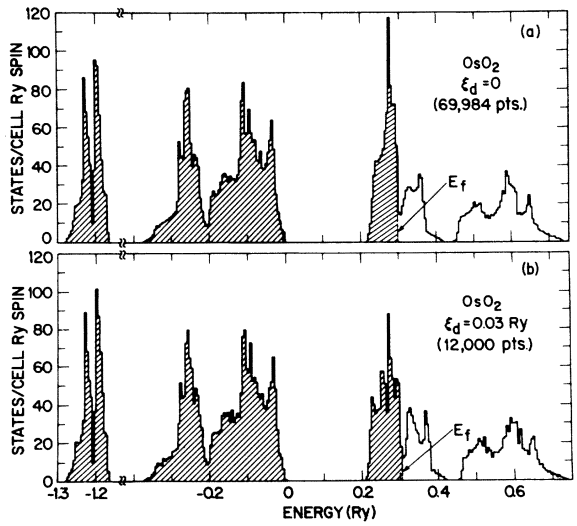

FIG. 8. $N(E)$ curves for OsO_2 with (a) $\xi_{5d}=0$; (b) $\xi_{5d}=0.03$ Ry.

At the moment, the Fermi-surface data of Graebner *et al.*[7] (GGR) provide the most direct means for evaluating the accuracy of the present energy-band results for these compounds. An interesting feature of the IrO_2 Fermi-surface results is the fact that it provides an indirect means for estimating the energy separation between the oxygen $2s$-$2p$ and the iridium $5d$ bands within the framework of the present APW-LCAO band model.

In interpreting their magnetothermal-oscillation (MTO) data, GGR have utilized the results of a preliminary APW-LCAO calculation for RuO_2 along symmetry lines in the Brillouin zone. They found that by adjusting the relative ordering of a few key energy-band states near E_F, they could obtain a Fermi-surface model for each compound that explained the majority of their data. The dimensions and shapes of these semiempirical Fermi-surface models are shown in the third column of Fig. 10. In each case, it is found that this semiempirical model is in good qualitative agreement with corresponding theoretical one involving spin-orbit cou-

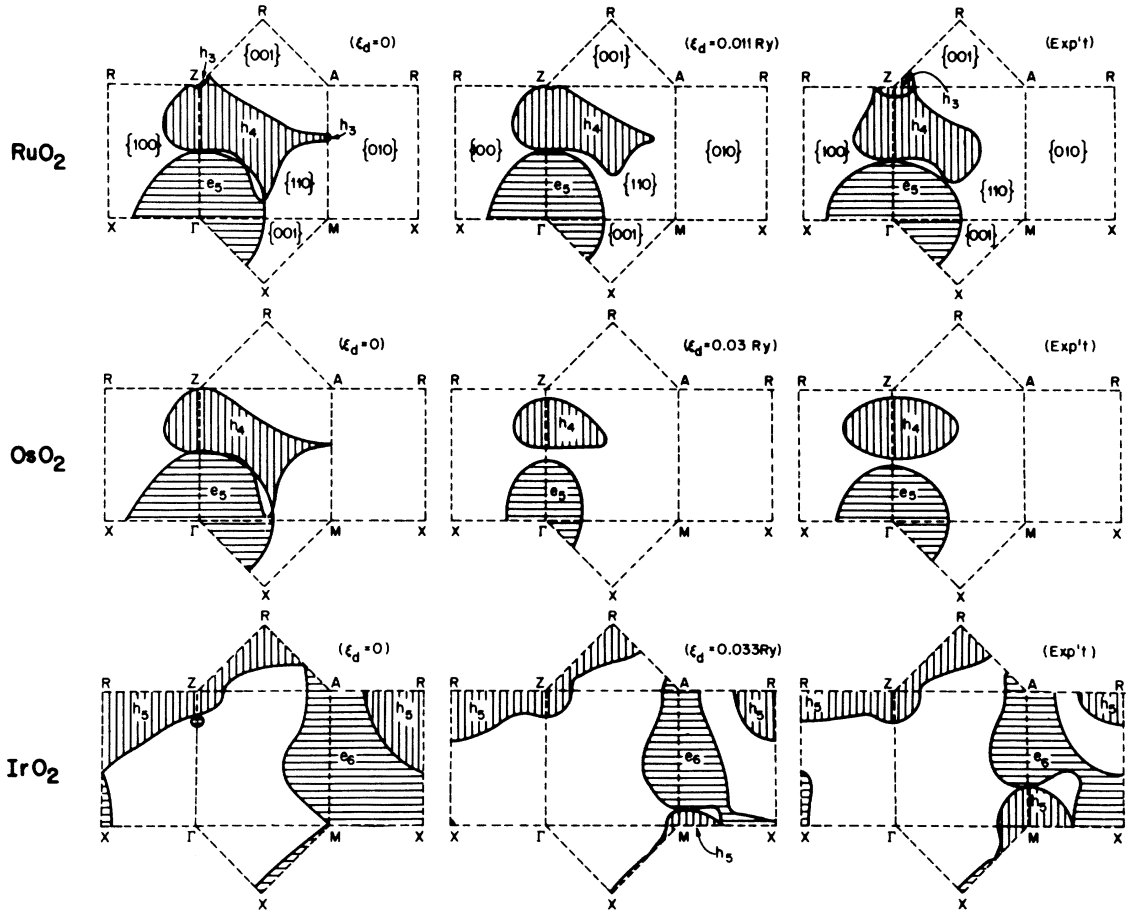

FIG. 10. Comparison of calculated Fermi-surface cross sections for RuO_2, OsO_2, and IrO_2 with those derived from magnetothermal-oscillation data by GGR.

pling (second column of Fig. 10).

The present Fermi-surface results support the over-all interpretation by GGR of their MTO data for these compounds. The interested reader is referred to the preceding paper[7] for the details of this interpretation. We limit our comments here to a few specific aspects of these data and its implications concerning the accuracy of various features of the present energy-band model.

We consider first the theoretical and experimental Fermi-surface results for RuO_2. The calculations predict that the fourth-band hole surface h_4 does not contact the zone boundary at Z, but just touches it along the ZA and ZR lines. The data of GGR suggest that the energy of the Z_2 state near E_F in Fig. 2 should be about 0.01 Ry higher than shown. This would produce an ellipsoidal hole pocket h_3 at Z with approximately the observed dimensions when spin-orbit coupling is included. The results of high-field magnetoresistance studies indicate the presence of open orbits along [001] in RuO_2.[7] In terms of the present Fermi-surface model, this requires that h_4 must contact both the zone boundary and e_5. There are three points of contact between h_4 and e_5 in a $\{110\}$ plane when $\xi_d = 0$. Spin-orbit coupling removes all three degeneracies. However, the spin-orbit gap between e_5 and h_4 along the ΓZ line in Fig. 10 is particularly small because of an accidental band crossing just below E_F so that magnetic breakdown is possible near this line.

A three-dimensional sketch of the theoretical RuO_2 Fermi surface is shown in Fig. 11. Unlike the semiempirical model of GGR, it is found that the $\{110\}$ arms of h_4 are smoothly tapered. In addition, h_4 intersects the [001] Brillouin-zone boundary with finite slope, producing a cusplike neck. This would explain the absence of neck orbits in the MTO data. The protrusions of h_4 toward the AM line in the $\{110\}$ plane provide a possible explanation of the $\alpha\beta$ MTO frequency that is observed when the magnetic field is near [001] in a $\{110\}$ plane. If this protrusion occurred at a lower value of k_z than the e_5-h_4 point of contact, then noncentral extremal orbits could exist on the arms of h_4 for all field orientations in a $\{110\}$ plane. As

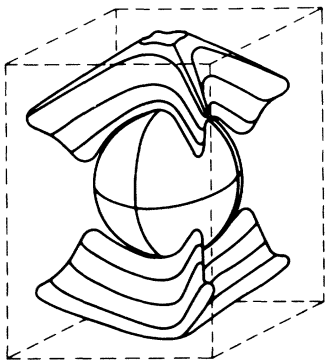

FIG. 11. Three-dimensional sketch of the RuO_2 Fermi surface.

discussed in the preceding section, this type of error is quite likely in the rutile structure, where there are three independent t_{2g} bands. According to the results of Fig. 2, the value of k_z at which e_5 and h_4 contact is determined by the intersection of the $(t_{2g})_2$ subband with E_F while that of the h_4 protrusion involves a crossing of the $(t_{2g})_2$ and $(t_{2g})_3$ subbands along the AM line near E_F.

Slivka and Langenberg[6] have observed Azbel-Kaner cyclotron resonance in RuO_2 single-crystal samples. Their data include a plot of the cyclotron effective mass as a function of $\vec{H}$ in a $\{110\}$ plane. They tentatively identify these masses with the de Haas–van Alphen frequency F_2 of Marcus and Butler.[3] In terms of the present notation, this corresponds to electron orbits on e_5. If one compares the angular variation of these masses with that of the α, β, and $\alpha\beta$ MTO frequencies of GGR, then it appears quite likely that these cyclotron effective masses are associated with noncentral orbits on the arms of h_4. We have not attempted to calculate theoretical values for these cyclotron masses because of the low symmetry of the surface involved.

According to the results of Fig. 10, the present APW-LCAO model underestimates the dimension of e_5 along the ΓX and ΓM directions in both RuO_2 and OsO_2. This discrepancy is increased by the effects of spin-orbit coupling. It is believed that these deficiencies are primarily due to small errors in the relative energies of the t_{2g} subbands. We have attempted to minimize these deficiencies in the present band-structure results for OsO_2 by arbitrarily reducing the osmium spin-orbit parameter by 20% from the Herman-Skillman atomic value.[22] A similar adjustment is also applied to IrO_2 in order to obtain the correct Fermi-surface topology in the vicinity of the X and M points of the Brillouin zone.

The main discrepancies between the calculated and experimental Fermi-surface dimensions for IrO_2 are readily traced to the relatively small bandwidth (0.013 Ry) between the $M_{3^+}M_{4^+}$ and X_1 states near E_F in Fig. 4. This discrepancy is somewhat unexpected since it involves primarily states within the $(t_{2g})_3$ subband. It is found that spin-orbit coupling increases the energy of the X_1 state more than that of $M_{3^+}M_{4^+}$ so that this bandwidth is reduced to 0.002 Ry for $\xi_{5d} = 0.033$ Ry and zero for $\xi_{5d} = 0.041$ Ry. On the other hand, the experimental Fermi-surface results of GGR imply an over-all bandwidth of 0.02–0.03 Ry.

A careful study of the LCAO model reveals that this $M_{3^+}M_{4^+} - X_1$ bandwidth is rather sensitive to the p-d energy separation via overlap-covalency interactions. It is found that this bandwidth is doubled if the d-orbital energy E_d in Table VII is reduced by 0.1 Ry. The resulting adjusted band structure and Fermi-surface dimensions for IrO_2 are shown in Fig. 12. It is clear that this adjusted LCAO band model for IrO_2 provides a rather accurate description of the observed Fermi-surface results shown in Fig. 10. It seems likely that a truly quantitative fit to the MTO data can be achieved by treating both ξ_d and E_d as adjustable parameters in the fitting procedure.

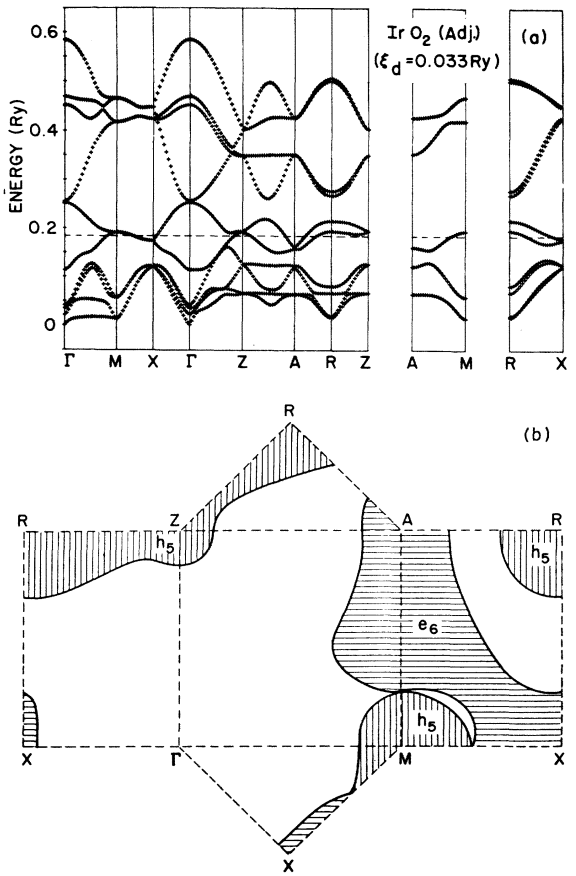

FIG. 12. (a) Adjusted LCAO bands for IrO_2 with E_d reduced by 0.1 Ry. (b) Calculated Fermi-surface cross sections derived from the above band structure.

We note that some of the apparent discrepancies between the adjusted and experimental Fermi-surface dimensions for IrO_2 are the result of simplifying assumptions in determining the latter. For example, GGR assume a spherical cross section to estimate the dimension of the neck joining the e_6 pockets at A and X in Fig. 10. The neck dimensions in Fig. 12 are also consistent with these data provided its thickness is about one third its width. This is not unreasonable since this neck is formed by a relatively flat band that is never more than 2 mRy below E_F.

The results of high-field magnetoresistance studies by Ryden *et al.*[5] on IrO_2 confirm many features of the GGR Fermi-surface results. The anisotropy of the monotonic magnetoresistance accounts for all the open orbits that are expected in terms of the GGR Fermi-surface model for IrO_2. In addition, the oscillatory magnetoresistance data confirm the assignment of MTO frequencies at the X, M, and A points of the Brillouin zone since it is found that coupled orbits resulting from the $h_5 - e_6$ degeneracies along MX and MA produce frequencies that are the sums of individual orbit frequencies.

Passenheim and McCollum[9] have measured the low-temperature heat capacities of RuO_2 and IrO_2 and have determined the electronic contribution γ. Neglecting the effects of electron-phonon enhancement, these γ values correspond to $N(E_F) = 33.2$ (RuO_2) and 31.7 (IrO_2) in units "states/cell-Ry-spin" of Figs. 7–9. The calculated values for the band density of states for RuO_2 are 21.5 ($\xi_d = 0$) and 25.7 ($\xi_d = 0.011$ Ry) while those for IrO_2 are 28.8 ($\xi_d = 0$) and 27.5 ($\xi_d = 0.033$ Ry) in these units. These results indicate that the electron-phonon enhancement factors $(1+\lambda)$ are fairly small in these compounds. This is consistent with the fact that superconductivity has not been observed in any of these materials.

V. DISCUSSION

One of the more interesting features of the present APW-LCAO results for these rutile-type compounds is the presence of the huge narrow peak in the conduction-band density of states. The height and width of this band density-of-states peak is comparable to that inferred from heat-capacity and susceptibility measurements for the high-temperature superconducting $A15$ compounds such as V_3Si and Nb_3Sn.[27] As discussed in Sec. III, this density-of-states peak arises from the relatively flat bands of the $(t_{2g})_1$ subband, particularly for wave vectors in and near the ZAR plane of the Brillouin zone. We have shown in Figs. 7–9 that the effects of spin-orbit coupling tend to wash out this very narrow peak in the density of states, especially in the $5d$ compounds OsO_2 and IrO_2. Consequently, we expect this peak to be particularly sharp in the $3d$ dioxides where ξ_d is small.

In order to check the identification of this peak in the density of states with the $(t_{2g})_1$ subband, we have calculated the partial density of states for each of the e_g and t_{2g} subbands of Table III. The results of this calculation for the RuO_2 band structure are shown in Fig. 13. In this calculation, each LCAO eigenvalue is weighted by the sum of squares of the appropriate eigenvector coefficients. When orbital overlap is included, the appropriate weighting factor is the atomic population of Mulliken[28] where the overlap charge is equally distributed among each pair of atoms. Instead, we have used the eigenvectors derived from Löwdin's symmetric orthogonalization scheme,[18,29] which are similar in magnitude to these atomic populations and always positive.

The uppermost curve shown in Fig. 13 represents the total Ru $4d$ density of states; the lowest curve is that of the oxygen $2p$ states. The intermediate curves correspond to the e_g and t_{2g} subbands. The oxygen $2s$ component is not shown since it closely resembles the curves shown in Fig. 7 in the energy range -1.3 to -1.2 Ry and its magnitude is less than 1 state/cell-Ry-spin elsewhere. According to the uppermost curve, the

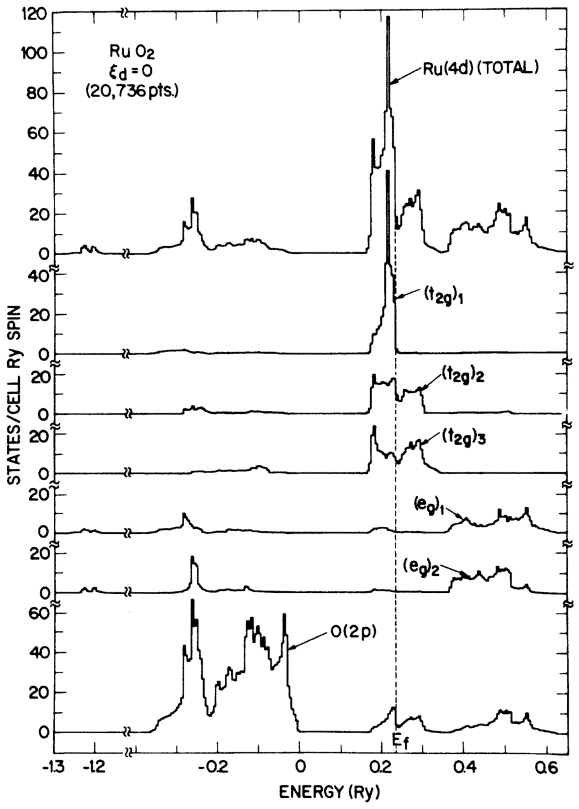

FIG. 13. Contributions of individual subbands to $N(E)$ for RuO_2.

Ru $4d$ charge density is distributed in energy range of the oxygen $2s$ and $2p$ bands because of the combined effects of orbital overlap and covalent mixing. The converse is true for the oxygen $2s$-$2p$ charge density. We note that the d component is largest near the bottom of the $2p$-band energy range, where its shape is a scaled replica of the total $2p$ density of states. This is precisely what one would expect in a covalently-bonded material. Most of the states in the energy range 0 to -0.2 Ry correspond to nonbonding oxygen $2p$ states. This situation is similar to that in ReO_3,[30] where the highest-energy peak in the oxygen $2p$ manifold is composed largely of nonbonding p states.

It is clear that the overlap and covalent mixing of the t_{2g} orbitals is significantly smaller than that of the e_g orbitals. This is consistent with the simple picture whereby t_{2g} orbitals form π bonds and e_g orbitals form σ bonds with the oxygen $2s$-$2p$ states. This is not rigorously true in a distorted octahedral environment, but it appears that it represents a reasonable approximation in the rutile structure. There exists relatively little hybridization between the e_g and t_{2g} subbands. In particular, these results confirm that the main peak in the conduction-band density of states is due mainly to the $(t_{2g})_1$ subband, which is 96% filled in RuO_2. It is clear from Fig. 13 that both the $(t_{2g})_2$ and $(t_{2g})_3$ subbands are roughly half-filled in this compound.

It is noted that the actual width of the $(t_{2g})_1$ subband (~ 0.05 Ry) is less than the over-all bandwidth shown in Fig. 5, where only d-d interactions are included. This phenomenon is readily understood in terms of "effective" d-d interaction parameters $\mathcal{E}_{\alpha,\beta}(\vec{r}_i)$.[19] In general, these effective interactions involve a combination of two terms. The first is a direct d-d interaction $E_{\alpha,\beta}(\vec{r}_i)$ while the second term involves indirect ligand-field-type contributions to the d bandwidth. Unexpectedly narrow bandwidths are possible in compounds where these two contributions very nearly cancel one another. Although we have not worked out the details, this is apparently the case for the $(t_{2g})_1$ subband in the rutile structure. We can illustrate the essential features of this phenomenon in terms of the results shown in Fig. 5. As discussed in Sec. III, the total $(3z^2 - r^2)$ bandwidth is essentially $4|(dd\sigma)_1|$ in the two-center approximation. If overlap-covalency effects raised the energy of the lowest pair of bands in the ΓXM plane of Fig. 5 but left the upper pair of bands unchanged in the ZRA plane, then the "effective" $(dd\sigma)_1$ parameter would be reduced by these ligand-field-type corrections. The actual situation is slightly more complicated in the rutile structure because the $(t_{2g})_1$ wave functions involve hybridized combinations of the $3z^2 - r^2$ and xy orbitals as well as covalent admixing.

It is clear from this and previous[19] discussions that these overlap-covalency interactions also change the average energies of the $(t_{2g})_n$ and $(e_g)_n$ subbands. These correspond to the "effective" parameters $\mathcal{E}_{\alpha,\alpha}(0, 0, 0)$, which can be determined by means of a least-squares fit to the metal-atom d bands with all overlap-covalency parameters set equal to zero. In this same way, one can also determine the corresponding parameters for the oxygen $2s$-$2p$ levels. As discussed previously,[19] these average energies represent the ligand-field levels of an isolated cluster.

The present APW-LCAO band model has been applied to determine these ligand-field levels for RuO_2. The results are shown in Fig. 14. The levels shown on the left-hand side are the atomiclike LCAO parameters of Table VII. For simplicity, we have replaced the three independent $2p$ orbital energies (E_{x+y}, E_{x-y}, and E_z) by their average value E_p. The effect of s-d and p-d overlap and covalency on these atomiclike levels is shown on the right-hand side. The octahedral component of the ligand field splits the fivefold-degenerate d level E_d into $\mathcal{E}(e_g)$ and $\mathcal{E}(t_{2g})$ sublevels. Finally, the orthorhombic component of the ligand field causes a further splitting of the $\mathcal{E}(e_g)$, $\mathcal{E}(t_{2g})$, and $\mathcal{E}_p$ levels. It is noted that $E_{x+y} \approx \mathcal{E}_{x+y}$, which implies that these orbitals are essentially nonbinding with respect to interactions with the Ru d orbitals. In addition, it is found that the shifts in the average energies of the antibonding (d-type) states is greater than those for the bonding (s-p-type) combinations.

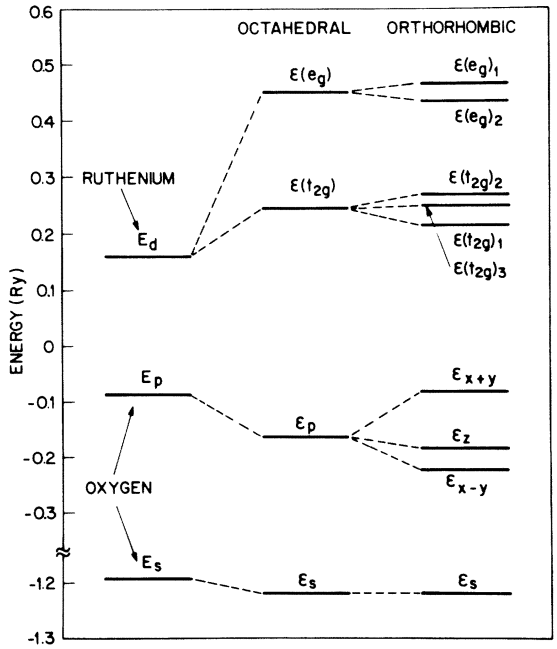

FIG. 14. Ligand-field splittings of Ru $4d$ and O $2s$-$2p$ levels, first in a octahedral environment, then with an orthorhombic distortion.

The position of the $(t_{2g})_1$ peak in the density of states relative to the Fermi energy provides an attractive explanation for the tendency of the d^1, d^2, and d^3 dioxides to distort (Table I). Preliminary calculations for the 3*d* dioxides show that the position of this peak relative to the $(t_{2g})_2$ and $(t_{2g})_3$ subbands and E_F depends on the c/a ratio. These effects will be discussed in more detail in a future publication dealing with the application of the present APW-LCAO band model to TiO_2, VO_2, and CrO_2. However, it is reasonable to expect that those compounds for which this density-of-states peak occurs near E_F would be unstable to Jahn-Teller-type distortions, not unlike those which have been proposed to explain the cubic-to-tetragonal transformation in V_3Si and Nb_3Sn.[27] On the basis of the present calculations, it seems unlikely that PtO_2 would fall into this category. However, we do note that the energy-band results of Figs. 2–4 suggest the likelihood that stoichiometric PtO_2 samples would exhibit semiconducting rather than semimetallic behavior.

Most previous theoretical discussions of the electronic properties of rutile-type compounds have focused on the 3*d* dioxides, particularly VO_2. Hyland[31] has applied electron-spin-resonance data on TiO_2 samples with substitutional V impurities to estimate the relative ordering of the e_g and t_{2g} levels of the V^{4+} ion in an orthorhombic environment. He obtains an ordering of the V $(e_g)_n$ and $(t_{2g})_n$ levels which is identical with that shown in Fig. 14. The relative splittings of the various levels are also quite similar in magnitude to those derived from the present RuO_2 band structure.

Goodenough[32] has proposed a schematic energy-band model for tetragonal VO_2. This model is entirely consistent with the over-all features of the density-of-states results in Fig. 13 for RuO_2. Goodenough's orbitals $f_{z^2-y^2}$, f_{zx}, f_{xy}, $f_{3x^2-r^2}$, and f_{yz} correspond to $(t_{2g})_1$, $(t_{2g})_2$, $(t_{2g})_3$, $(e_g)_1$, and $(e_g)_2$ of Table III, respectively. The $(t_{2g})_1$ subband is denoted by $d_{\|}$ while the $(t_{2g})_2$ and $(t_{2g})_3$ subbands are labeled π^* in Goodenough's notation. These are separated by a small gap from the σ^* or $(e_g)_1$ and $(e_g)_2$ subbands. The future application of the present APW-LCAO band model to VO_2 will permit a detailed evaluation of Goodenough's schematic band model for this compound, particularly its generalization to treat the metal-insulator transition that is observed at 340 °K.

ACKNOWLEDGMENTS

I wish to acknowledge many useful conversations with J. H. Condon, J. E. Graebner, W. A. Reed, and W. D. Ryden regarding the experimental data for these rutile-type compounds and their interpretation. I am grateful to J. A. Wilson for suggesting several improvements in the manuscript.

[1]J. B. Goodenough, in *Progress in Solid State Chemistry*, edited by H. Reiss (Pergamon, Oxford, 1971), Vol. 5.
[2]D. Adler, in *Solid State Physics*, edited by F. Seitz, D. Turnbull, and H. Ehrenreich (Academic, New York, 1968), Vol. 21; Rev. Mod. Phys. 40, 714 (1968).
[3]S. M. Marcus and S. R. Butler, Phys. Lett. A 26, 518 (1968).
[4]S. M. Marcus, Phys. Lett. A 28, 191 (1968).
[5]W. D. Ryden, W. A. Reed, and E. S. Greiner, Phys. Rev. B 6, 2089 (1972).
[6]R. T. Slivka and D. N. Langenberg, Phys. Lett. A 28, 169 (1968).
[7]J. E. Graebner, E. S. Greiner, and W. D. Ryden (preceding paper) Phys. Rev. B 13, 2426 (1976); J. E. Graebner and W. D. Ryden, Bull. Am. Phys. Soc. 15, 312 (1970).
[8]W. D. Ryden, A. W. Lawson, and C. C. Sartain, Phys. Rev. B 1, 1494 (1970).
[9]B. C. Passenheim and D. C. McCollum, J. Chem. Phys. 51, 320 (1969).
[10]J. C. Slater and G. F. Koster, Phys. Rev. 94, 1498 (1954).
[11]E. Caruthers, L. Kleinman, and H. I. Zhang, Phys. Rev. B 7, 3753 (1973).
[12]S. Chatterjee, T. K. Mitra, and G. J. Hyland, Phys. Lett. A 42, 56 (1972).
[13]C. E. Boman, Acta. Chem. Scand. 24, 116 (1970); 24, 123 (1970).
[14]C. L. McDaniel and S. J. Schneider, J. Res. Natl. Bur. Stand. (U.S.) A 71, 119 (1967).
[15]L. P. Bouckaert, R. Smoluchowski, and E. Wigner, Phys. Rev. 50, 58 (1936).
[16]J. O. Dimmock and R. G. Wheeler, Phys. Rev. 127, 391 (1962).
[17]J. G. Gay, W. A. Albers, Jr., and F. J. Arlinghaus, J. Phys. Chem. Solids 29, 1449 (1968).
[18]L. F. Mattheiss, Phys. Rev. 181, 987 (1969); Phys. Rev. B 2, 3918 (1970).
[19]L. F. Mattheiss, Phys. Rev. B 5, 290 (1972); 5, 306 (1972).
[20]L. F. Mattheiss, Phys. Rev. B 6, 4718 (1972).
[21]L. F. Mattheiss, Phys. Rev. B 8, 3719 (1973).
[22]F. Herman and S. Skillman, *Atomic Structure Calculations* (Prentice-Hall, Englewood Cliffs, N.J., 1963).
[23]J. C. Slater, Phys. Rev. 81, 385 (1951).
[24]W. B. Pearson, *A Handbook of Lattice Spacings and Structures of Metals and Alloys* (Pergamon, Edinburgh, 1964).
[25]R. F. Egorov, B. I. Reser, and V. P. Shirokovskii, Phys. Status Solidi 26, 391 (1968).
[26]T. K. Mitra, S. Chatterjee, and G. J. Hyland, Can. J. Phys. 51, 352 (1973).
[27]M. Weger and I. B. Goldberg, in *Solid State Physics*, edited by H. Ehrenreich, F. Seitz, and D. Turnbull (Academic, New York, 1973), Vol. 28.
[28]R. S. Mulliken, J. Chem. Phys. 23, 1833 (1955).
[29]P. O. Löwdin, J. Chem. Phys. 18, 365 (1950).
[30]G. K. Wertheim, L. F. Mattheiss, M. Campagna, and T. P. Pearsall, Phys. Rev. Lett. 32, 997 (1974).
[31]G. J. Hyland, J. Phys. C 1, 189 (1968).
[32]J. B. Goodenough, J. Solid State Chem. 3, 490 (1971).

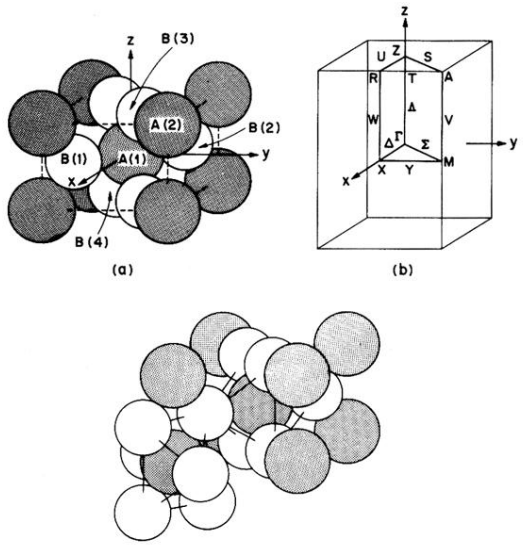

FIG. 1. (a) Primitive unit cell for AB_2 compounds with the rutile structure. (b) Brillouin zone for the tetragonal Bravais lattice with $c/a<1$. (c) Orientation of octahedral clusters surrounding A atoms at body-centered and corner positions.